

First-principles nonequilibrium dynamical cluster theory for quantum transport simulations of disordered nanoelectronic devices

Yu Zhang,^{1,2,3} Jianxiong Zhai,¹ Zhiyi Chen,¹ Qingyun Zhang,¹ and Youqi Ke^{1,2,3,*}

¹*School of Physical Science and Technology, ShanghaiTech University, Shanghai 201210, China*

²*Shanghai Institute of Optics and Fine Mechanics, Chinese Academy of Sciences, Shanghai 201800, China*

³*University of Chinese Academy of Sciences, Beijing 100049, China*

 (Received 3 June 2021; revised 30 August 2021; accepted 1 September 2021; published 13 September 2021)

As important progress for simulating realistic device materials, we report the first-principles nonequilibrium dynamical cluster theory for simulating the quantum transport properties of nanoelectronics with inevitable disordered defects or dopants. In this method, we formulate the nonequilibrium dynamical cluster theory in Keldysh's Green's function representation, and implement it with the exact muffin-tin orbital based density functional theory. With this method, the important correlation effects of disordered scattering and short-range order effects can be effectively treated for the nonequilibrium electronic structure and quantum transport calculations of devices under finite bias. Moreover, a double-energy-contour technique is devised to considerably improve the numerical convergence in the nonequilibrium electron structure calculation. As the demonstration, the first-principles nonequilibrium dynamical cluster theory is applied to calculate Cu/Co junction with disordered interface and Fe/vacuum/Fe magnetic tunnel junction with surface roughness. We find that a sizable transmission decrease can be induced by including the correlation effects of disorders of few layers in the Cu/Co junction, presenting the important transport channel closing due to disordered quantum interference. For Fe/vacuum/Fe junction, we find that short-range order of surface roughness, with the important clustering and anticlustering tendencies, can dramatically change the transmission properties compared to the case of (or close to) complete randomness. The development of first-principles nonequilibrium dynamical cluster theory provides an important approach for analyzing the process-dependent device performance, extending the capability of first-principles quantum transport simulation.

DOI: [10.1103/PhysRevB.104.115412](https://doi.org/10.1103/PhysRevB.104.115412)

I. INTRODUCTION

The presence of disordered defects or intentional dopants can significantly influence or even determine the material properties and device functionalities, especially at the nanoscale. [For example, a small amount of interfacial disorders in Fe/MgO/Fe magnetic tunneling junction (MTJ) can greatly decrease the tunneling magnetoresistance ratio by orders of magnitude [1,2]]. It is known that disorder can dramatically change the carrier transport from ballistic to diffusive, and even to weak or full localization regime in metallic wires. Moreover, due to the lack of self-averaging, nanoscale field effect transistors present the important random dopant fluctuation, giving rise to large device-to-device variability which presents great challenge for device fabrication. Therefore, developing simulation methods to effectively treat the important effects of inevitable disorders is critical for process and materials design in modern device researches. Coherent potential approximation(CPA) [3,4] as an effective mean field theory for disorder average presently has important applications (combining with first-principles methods) in calculating electronic structure and mechanical properties of alloys [5–11] and simulating the quantum transport properties

of disordered nanoelectronic and spintronic devices [1,2,12–16]. CPA constructs an effective medium with translational symmetry self-consistently to obtain the disorder-averaged physical quantities. CPA is conventionally implemented in the single-site approximation [17], which ignores the nonlocal correlation of disorders (even neighboring). As a result, conventional CPA is suitable for the quenched-type disorder system, featuring complete randomness, with weak scattering and nonlocal correlation. However, in alloys with large concentration and strong scattering, the cluster effect, namely nonlocal correlations, is important for device and materials' property, especially towards weak and full localization regime. Moreover, in realistic devices' and materials' fabrication, atomic relaxation due to the annealing process can result in disorders with short-range order, in contrast to the quenched disorder. It has been first found that, because of the important short-range order (SRO) effects, the resistivity of Ti-Al alloys presents important differences between samples annealed at different temperatures [18–20]. The relaxation of defects has been found to present significant influences on the transport properties of two-dimensional (2D) materials [21]. The presence of SRO is beyond the capability of the single-site CPA. It is therefore desirable to develop simulation methods to realize the analysis of the SRO effects for both device and process designs in modern semiconductor technology.

*keyq@shanghaitech.edu.cn

Presently, there are two mainstream methods to account for (to some extent) the important correlations of disorders, including supercell (SC) methods and the cluster mean-field theories, which can approach exact results in the limit of infinite supercell or cluster size. The supercell methods, doing the disorder average by calculating different random or quasirandom configurations [22] in a finite supercell with periodic boundary condition, have present important applications in combination with first-principles methods. However, the applicability of SC methods is always limited by the large computational cost and finite supercell size. On the other hand, cluster mean-field theories provide effective approaches to include the spatial correlation within the cluster. As a straightforward extension of CPA, by replacing the single site with a cluster or molecule, molecular CPA (MCPA) is proposed [23,24] to deal with correlation effects inside the cluster. MCPA preserves the translational symmetry of the cluster, but fails to conserve the full symmetry of the lattice [25]. To restore the full symmetry, an elegant method called dynamical cluster approximation (DCA), which was originally proposed by Hettler *et al.* [26] (with the analyticity proved in Ref. [27]) for describing the nonlocal dynamical correlations in correlated electron systems, has been applied to account for the correlation effects in atomically disordered materials [28] (there exists different name as nonlocal CPA (NLCPA) [29,30]). Recently, the success of DCA for disordered system has been demonstrated with the tight-binding models, including site-diagonal disorder [31–33], combination with Blackman-Esterling-Berk [34] transformation for off-diagonal disorder [35], and with dual-fermion technique to include nonlocal correlations [36] and with typical medium theory for Anderson localization [37–40]. By applying the periodic Born–von Karman (BVK) boundary conditions to the cluster, DCA preserves the full translational and point-group symmetries of the lattice. The DCA self-energy, describing the effective medium of disorder average, can be calculated for several different K points in the Brillouin zone (BZ) of the primitive cell, beyond the self-energy of single-site CPA calculated only at the Γ point. Different from the SC method [41,42] and MCPA, DCA limits the computational cost at the level of the primitive cell, which makes it feasible to combine with first-principles simulations. Presently, combing DCA or NLCPA with density functional theory (DFT) [43,44], for example, KKR-NLCPA [30,45–47], provides an important first-principles approach for simulating realistic alloys, and has presented important applications in bulk systems (such as the resistivity of CuZn and AgPd alloys with SRO effects) [48]. However, the nonequilibrium DCA simulation of disordered nanoelectronic devices has not been reported yet, while disorders play important roles in the performance of realistic device. In this paper, we report the approach of the DCA in combination with nonequilibrium Green’s function (NEGF) method and DFT to realize the first-principles quantum transport simulation of the disordered nanoelectronic devices. With this method, the important correlation effects of disorder and SRO effects can be explicitly accounted for the electron transport calculations. The DFT-NEGF-DCA approach is implemented within the framework of exact muffin-tin orbital method (EMTO) [8,10,49–51], which features the high localization and minimal basis. To demonstrate our

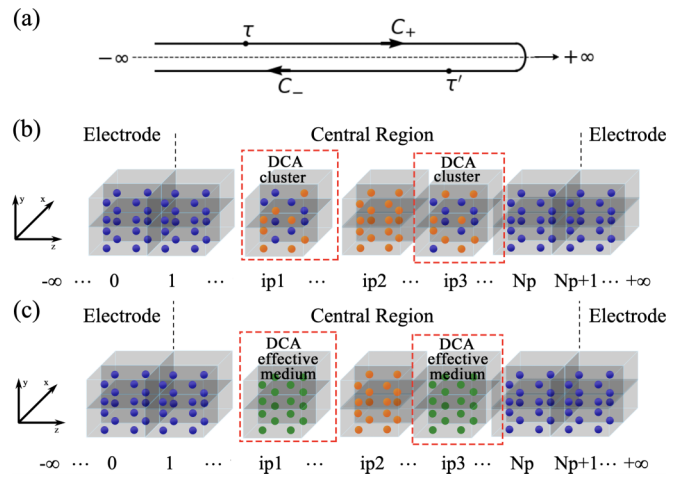


FIG. 1. (a) The Schwinger-Keldysh closed-time contour: starts from $-\infty$, passes through τ and τ' , and finally returns to $-\infty$. There are four real-time quantities $Q^{i,i>,<}(\tau, \tau')$ with τ and τ' on the two branches C_+ or C_- . (b) Schematic illustration of a disordered two-probe device. The device is divided into different principal layers labeled by ip and contains clean left electrode $ip \leq 0$, disordered central region $1 \leq ip \leq N_p$, and clean right electrode $ip \geq N_p + 1$. The disordered sites are included in different DCA clusters. (c) Schematic illustration of disorder-averaged two-probe device with the DCA effective medium.

implementation of EMTO-DFT-NEGF-DCA, we calculate the disorder correlation effect on the transmission of Cu/Co junction with disordered interfacial interdiffusion, and the SRO effect on the spin-dependent tunneling in Fe/vacuum (Va)/Fe MTJ with disordered surface roughness.

This paper is organized as follows: In Sec. II, we review NEGF based quantum transport algorithm and EMTO method for nanoelectronic device simulation. In Sec. III, we formulate the DCA with the Keldysh’s nonequilibrium Green’s function representation within EMTO. In Sec. IV, we introduce the implementation of EMTO-DFT-NEGF-DCA method for the self-consistent nonequilibrium electronic structure and transport calculation. In Sec. V, we present the transport results for disordered Cu/Co junction and Fe/Va/Fe MTJ. Finally, we conclude our work in Sec. VI and provide more information in the Appendix.

II. NONEQUILIBRIUM GREEN’S FUNCTION TECHNIQUE FOR QUANTUM TRANSPORT SIMULATION WITH EXACT MUFFIN-TIN ORBITAL METHOD

We consider an operating two-probe device-material system, containing a central region (with disorders) sandwiched by two semi-infinite electrodes [as shown in Fig. 1(b)], and the electron current flow is driven by applying a bias voltage. To treat such a quantum transport problem, the nonequilibrium Green’s function (NEGF) technique provides a general approach to deal with the nonequilibrium quantum statistics [52,53]. The central quantity in NEGF theory is the contour-ordered Green’s function (GF) defined on the closed-time contour, for example, Schwinger-Keldysh contour as shown in Fig. 1(a) [52]. With the Keldysh’s rotation [54,55], the contour-ordered Green’s function (GF) can be represented in

the form of a real-time Keldysh's 2×2 matrix, namely,

$$\mathbf{G} = \begin{pmatrix} G^A & 0 \\ G^K & G^R \end{pmatrix}, \quad (1)$$

where $G^{\mathcal{R}/A/K}$ are the respective retarded, advanced, and Keldysh's GFs. (Note that all the quantities in bold font in this paper are contour-ordered quantities in the Keldysh's representation). As the advantage of being defined on the closed-time contour, the NEGF in Eq. (1) satisfies the Dyson equation, just like the equilibrium GF. As a result, to calculate the NEGF of the central device region interested, namely \mathbf{G}_c , the influence of electrodes can be treated as the self-energy such that

$$\mathbf{G}_c = \mathbf{G}_{c0} + \mathbf{G}_{c0} \boldsymbol{\Sigma}_{\text{id}} \mathbf{G}_c, \quad (2)$$

where $\boldsymbol{\Sigma}_{\text{id}}$ denotes the self-energy of electrodes, and \mathbf{G}_{c0} is the GF of isolated central region, making the infinite device calculable. Here, we consider the device in steady state, then both the GF and self-energy can be Fourier transformed from the time to energy domain, namely, $\mathbf{G}(\epsilon, \vec{r}, \vec{r}')$ and $\boldsymbol{\Sigma}_{\text{id}}(\epsilon, \vec{r}, \vec{r}')$.

With the three GFs in the Keldysh's representation including $G^{\mathcal{R}/A/K}$, the lesser and greater GFs, namely $G_c^{>/<}$, could be obtained straightforwardly by the relations [14]

$$\begin{aligned} G_c^< &= \frac{1}{2}(-G_c^{\mathcal{R}} + G_c^A + G_c^K), \\ G_c^> &= \frac{1}{2}(-G_c^A + G_c^{\mathcal{R}} + G_c^K), \end{aligned} \quad (3)$$

with the important relation $G_c^A - G_c^{\mathcal{R}} = G_c^< - G_c^>$.

Then with these different GFs, many important physical properties of the central region can be calculated, for example, the nonequilibrium electron density directly given by

$$\rho_c(\vec{r}) = \int \frac{1}{2\pi} \text{Im}[G_c^<(\epsilon, \vec{r}, \vec{r})] d\epsilon, \quad (4)$$

the spectral function

$$A_c(\epsilon) = i(G_c^A(\epsilon) - G_c^{\mathcal{R}}(\epsilon)), \quad (5)$$

and the electron current flowing through the device (given by Meir-Wingreen formula) [56]

$$\begin{aligned} I &= \frac{ie}{2h} \int_{-\infty}^{\infty} d\epsilon \text{Tr} \{ [f_L(\epsilon) \Gamma_L(\epsilon) - f_R(\epsilon) \Gamma_R] [G_c^{\mathcal{R}} - G_c^A] \} \\ &+ \text{Tr} \{ [\Gamma_L - \Gamma_R] G_c^< \}, \end{aligned} \quad (6)$$

where $f_{L/R}(\epsilon)$ and $\Gamma_{L/R} \equiv i[\Sigma_{\text{id},L/R}^{\mathcal{R}} - \Sigma_{\text{id},L/R}^A]$ are the respective Fermi function and linewidth function of left and right electrodes.

The combination of NEGF technique with first-principles DFT method, since the first report by Taylor *et al.* [57], have been established as the work-horse approach for quantum transport simulation of real device materials [2,12,13,15,16,57–66]. In our previous works, we have reported the exact muffin-tin orbital (EMTO) based as the first-principles simulation of electron and spin quantum transport with the scalar and full relativistics [15,16]. EMTO, as the third-generation MTO method, features the high accuracy and efficiency, desired for the simulation of device structures (which is usually much larger than the bulk in cell size). EMTO method utilizes the overlapped muffin-tin

potential approximation to improve the accuracy, and an important screening technique to make the basis highly localized [67]. As another important advantage, EMTO method can be combined with CPA to effectively treat effects of disorder scattering on electron and spin transport [8,10,15,16]. The EMTO, as an energy-dependent atom-centered basis [10], is constructed as

$$\Phi_{RL}^a(\epsilon, \mathbf{r}_R) = \phi_{RL}^a(\epsilon, \mathbf{r}_R) - \varphi_{RL}^a(\epsilon, \mathbf{r}_R) + \psi_{RL}^a(\epsilon, \mathbf{r}_R), \quad (7)$$

where a donates the screening representation, and ϕ_{RL} , φ_{RL} , and ψ_{RL} are the respective partial wave, free-electron solution, and screened spherical wave. Within the EMTO method, the overlap and Hamiltonian matrices can be analytically derived to obtain

$$\langle \Phi | \epsilon - H | \Phi \rangle = aS^a(\epsilon) - aD(\epsilon) \equiv K(\epsilon), \quad (8)$$

where potential function D is the onsite quantity determined by the atom of each site, the screened slope matrix S^a only depends on the structure and is highly sparse, providing the basis for highly efficient calculation of GFs. As a result, within the framework of EMTO, the NEGF for the central device in Eq. (2) can be rewritten as

$$\mathbf{G}_c = [aS_c^a - a\mathbf{D}_c - \boldsymbol{\Sigma}_{\text{id},L} - \boldsymbol{\Sigma}_{\text{id},R}]^{-1}, \quad (9)$$

where $\Sigma_{\text{id},L/R}^{\mathcal{R}} = K_{cL/cR}^{\mathcal{R}} K_{LL/RR}^{\mathcal{R}}^{-1} K_{Lc/Rc}$, $\Sigma_{\text{id},L/R}^A = \Sigma_{\text{id},L/R}^{\mathcal{R} \dagger}$, $\Sigma_{\text{id},L/R}^K = (1 - 2f_{L/R}(\epsilon))(\Sigma_{\text{id},L/R}^{\mathcal{R}} - \Sigma_{\text{id},L/R}^A)$, $S^A = S^{\mathcal{R} \dagger}$, $D^A = D^{\mathcal{R} \dagger}$, and $S^K = D^K = 0$. With the above Keldysh's NEGF, the physical properties of materials and devices can be efficiently calculated with the EMTO method [15,16]. In the practical implementation, we divide the two-probe device into different principal layers (PLs) (as shown in Fig. 1, the central device region contains PLs $1 \leq ip \leq N_p$, while the left and right electrodes contain PLs $ip \leq 0$ and $ip \geq N_p + 1$, respectively). The size of each PL is chosen so that the kink matrix K becomes block tridiagonal. For a perfect device system, which is periodic in the x - y plane perpendicular to the nonperiodic transport z direction, we apply the 2D lattice Fourier transformation and recursive GF method [15,68,69].

III. NONEQUILIBRIUM DYNAMICAL CLUSTER APPROXIMATION IN KELDYSH'S REPRESENTATION FOR DISORDERED SYSTEMS

We consider a device with atomic disorders presented in the central region [as shown in Fig. 1(b)]. For the NEGF in Eq. (9) within EMTO for a disordered device, the atom-dependent onsite quantity $\mathbf{D}_{c,R}$ becomes random, breaking the translational symmetry. To obtain physically meaningful results, the disorder average is required. To do so, one can introduce an effective medium to give the averaged NEGF in Keldysh's representation with EMTO, namely,

$$\tilde{\mathbf{G}}_c = [aS_c^a - a\tilde{\mathbf{D}}_c - \boldsymbol{\Sigma}_{\text{id},L} - \boldsymbol{\Sigma}_{\text{id},R}]^{-1}, \quad (10)$$

where $\tilde{\mathbf{D}}_c$ is the effective potential function describing the disorder-averaged medium. In the previous works with scalar and full relativistic EMTO [15,16], the single-site CPA in combination with vertex correction has been successfully implemented to solve $\tilde{\mathbf{D}}_c$, to obtain the averaged NEGF for the electron and spin transport through disordered devices.

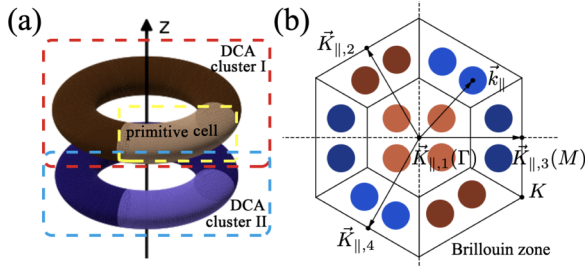


FIG. 2. (a) Schematic illustration of DCA cluster with Born-von Karman periodic boundary condition. (b) Schematic illustration of BZ partition for 2D BZ of fcc(111) plane when $N_{xy} = 4$. The 4 $\vec{K}_{\parallel,n}$ are marked in the 2D BZ, the points of \vec{k}_{\parallel} within the same coarse-grained region of \vec{K}_{\parallel} are denoted with the same color.

Despite single-site CPA features easy implementation, the associated $\tilde{\mathcal{D}}_c$ is site diagonal ($\tilde{\mathcal{D}}_{c,RR'} = 0$ for $R \neq R'$), suffering from the absence of nonlocal correlation and short-range order effects of disorders. To overcome the limitations of CPA, we here introduce the approach of combining dynamical cluster approximation with NEGF in EMTO to account for the disorder cluster effects on quantum transport, presenting an important step toward the first-principles simulation of realistic devices. Compared to the site-diagonal approximation in single-site CPA, the $\tilde{\mathcal{D}}_c$ in DCA has been developed to contain site-off-diagonal contribution to account for nonlocal correlation, and this is realized by calculating the $\tilde{\mathcal{D}}_c$ on a few coarse-grained \vec{K} in BZ by enforcing the Born-von Karman periodic boundary condition to the finite cluster [26]. To realize the DCA for the disordered two-probe device, the DCA cluster can be chosen to contain N_z number of disordered atomic layers along with nonperiodic transport z axis and N_{xy} number of primitive cells with BVK boundary condition in xoy plane as shown in Fig. 2(a). In such a way, the correlation could be fully considered within the $N_z \times N_{xy}$ disordered sites of the DCA cluster, while the correlation between different DCA clusters in transport z direction is neglected. One can group the different disordered atomic layers with important correlations into a single DCA cluster. It is clear that, when $N_z = N_{xy} = 1$, DCA is reduced to the single site CPA, and the DCA approaches the exact solution when N_z include all disordered layers in the device and $N_{xy} \rightarrow \infty$. Since the translational symmetry of the primitive cell (different from the MCPA) is restored in DCA after the disorder average, the GF in Eq. (10) could be rewritten with 2D Fourier transformation as

$$\tilde{\mathcal{G}}_c(\vec{k}_{\parallel}) = [a\mathcal{S}_c^a(\vec{k}_{\parallel}) - a\tilde{\mathcal{D}}_c(\vec{K}_{\parallel,n}) - \Sigma_{ld,L}(\vec{k}_{\parallel}) - \Sigma_{ld,R}(\vec{k}_{\parallel})]^{-1}, \quad (11)$$

where \vec{k}_{\parallel} is the k vector in 2D BZ of primitive lattice, and $\vec{K}_{\parallel,n}$ is the associated n th cluster momentum which is obtained by applying the Born-von Karman periodic boundary condition to the DCA cluster, namely, $\exp(i\vec{K}_{\parallel,n} \cdot \vec{L}_{\parallel,m}) = 1$, where $\vec{L}_{\parallel,m}$ is the cluster translational vector [26]. Here, the coarse-graining approximation $\tilde{\mathcal{D}}_c(\vec{k}_{\parallel}) = \tilde{\mathcal{D}}_c(\vec{K}_{\parallel,n})$ is applied when $\vec{k}_{\parallel} = \vec{K}_{\parallel,n} + \vec{\tilde{k}}_{\parallel}$ where $\vec{\tilde{k}}_{\parallel}$ is the k vector of 2D BZ for the superlattice of DCA cluster [46,47]. It is clear that, in DCA, the disorder effects are accounted by a set of

$\tilde{\mathcal{D}}_c(\vec{K}_{\parallel,n})$ with different $\vec{K}_{\parallel,n}$. With the nonlocal correlations, $\tilde{\mathcal{D}}_c(\vec{K}_{\parallel})$ contains nonzero site-off-diagonal elements, namely, $\tilde{\mathcal{D}}_{c,BB'}(\vec{K}_{\parallel}) \neq 0$ (B is the basis in primitive cell), when both B and B' are disordered sites within the same DCA cluster, while any site-off-diagonal elements associated with ordered sites are still zero. Thus, we divided $\tilde{\mathcal{D}}_c(\vec{K}_{\parallel,n})$ into two parts, namely, $\tilde{\mathcal{D}}_c(\vec{K}_{\parallel,n}) = \tilde{\mathcal{D}}_{c,\mathcal{P}}(\vec{K}_{\parallel,n}) + \mathcal{D}_{c,B}$. For the ordered sites, the site-diagonal part $\mathcal{D}_{c,B} = \sum_B \mathcal{D}_{c,B}$ is known, while all the elements $\tilde{\mathcal{D}}_{c,\mathcal{P}}(\vec{K}_{\parallel,n}) = \sum_p \tilde{\mathcal{D}}_{c,p}(\vec{K}_{\parallel,n})$, where $\tilde{\mathcal{D}}_{c,p}$ denotes the effective potential function for the p th DCA cluster, need to be solved in a self-consistent way to obtain the averaged GFs.

Within DCA, to form a set of self-consistent equations to determine $\tilde{\mathcal{D}}_{c,p}(\vec{K}_{\parallel,n})$ for different $\vec{K}_{\parallel,n}$, a quantity called coherent interactor $\Omega_p(\vec{K}_{\parallel,n})$ [70] is introduced to describe the influence of environment to the p th disordered DCA cluster, so that

$$\Omega_p(\vec{K}_{\parallel,n}) = [\tilde{\mathcal{G}}_{c,p}(\vec{K}_{\parallel,n})]^{-1} + a\tilde{\mathcal{D}}_{c,p}(\vec{K}_{\parallel,n}), \quad (12)$$

where $\tilde{\mathcal{G}}_{c,p}(\vec{K}_{\parallel,n})$ is given by the relation, namely, the coarse-graining approximation $\tilde{\mathcal{G}}_{c,p}(\vec{K}_{\parallel,n}) = \frac{1}{N_{\vec{k}_{\parallel}}} \sum_{\vec{k}_{\parallel}} \tilde{\mathcal{G}}_{c,p}(\vec{k}_{\parallel,n} + \vec{k}_{\parallel})$, where $N_{\vec{k}_{\parallel}}$ is the number of \vec{k}_{\parallel} . After solving the interactor Ω_p for all $\vec{K}_{\parallel,n}$, one can obtain a real-space interactor by the inverse Fourier transformation

$$[\Omega_p]_{RR'} = \frac{1}{N_{xy}} \sum_n e^{i\vec{K}_{\parallel,n} \cdot (\vec{T}'_{\parallel} - \vec{T}_{\parallel})} \Omega_{p,B,B'}(\vec{K}_{\parallel,n}), \quad (13)$$

where R, R' are different disordered sites in the DCA cluster ($R = B + \vec{T}_{\parallel}$ and $R' = B' + \vec{T}'_{\parallel}$), and \vec{T}_{\parallel} and \vec{T}'_{\parallel} are the translational vectors of primitive cell for sites in the DCA cluster. Because of the BVK boundary condition, the effective medium of DCA clusters in EMTO could be conceived as circles with closed boundary in xoy plane as shown in Fig. 2(a). Then, the NEGF for the p th DCA cluster with a specific disordered configuration \mathcal{Q} can be given as, in the real space,

$$\mathcal{G}_{c,p}^{\mathcal{Q}} = [\Omega_p - a\mathcal{D}_{c,p}^{\mathcal{Q}}]^{-1}, \quad (14)$$

where $\mathcal{D}_{c,p}^{\mathcal{Q}} = \sum_R \mathcal{D}_{c,p,R}^{\mathcal{Q}}$, and $\mathcal{D}_{c,p,R}^{\mathcal{Q}}$ is for the \mathcal{Q} element at site R for the configuration \mathcal{Q} in the p th DCA cluster. Then, the averaged GF of the DCA cluster is obtained by averaging over the results for all configurations

$$\tilde{\mathcal{G}}_{c,p} = \sum_{\mathcal{Q}} w^{\mathcal{Q}} \mathcal{G}_{c,p}^{\mathcal{Q}}, \quad (15)$$

where $w^{\mathcal{Q}}$ is the weight for each disorder configuration \mathcal{Q} of DCA cluster. Different from cluster GF in MCPA, $\tilde{\mathcal{G}}_{c,p}$ in DCA features the translational symmetry of the primitive lattice in the xoy plane. Once $\tilde{\mathcal{G}}_{c,p}$ is obtained, we can calculate the effective function $\tilde{\mathcal{D}}_{c,p}$ for the DCA cluster as

$$a\tilde{\mathcal{D}}_{c,p} = \Omega_p - [\tilde{\mathcal{G}}_{c,p}^{-1}]. \quad (16)$$

Then, by enforcing the Born-von Karman periodic boundary condition, the $\tilde{\mathcal{D}}_{c,p}(\vec{K}_{\parallel,n})$ in Eq. (11) on a set of discrete $\vec{K}_{\parallel,n}$ can be evaluated with the discrete Fourier transformation,

namely,

$$\tilde{\mathbf{D}}_{c,p,B,B'}(\vec{K}_{\parallel,n}) = \sum_{\vec{T}_{\parallel}} e^{-i\vec{K}_{\parallel,n}\cdot\vec{T}_{\parallel}} [\tilde{\mathbf{D}}_{c,p}]_{B,B'+\vec{T}_{\parallel}}. \quad (17)$$

By here, Eqs. (11)–(17), with all quantities in bold defined in Keldysh's representation, form a closed set of DCA self-consistent equations for solving the averaged NEGF. Here, the cluster solver consists of Eqs. (14) and (15) in which a number of atomic configurations with complete randomness or short-range order can be considered. The iterative calculation starts with an initial guess of a coherent interactor Ω_p ; and then, with the cluster solver, we solve the effective potential function $\tilde{\mathbf{D}}_{c,p}$ to generate the new NEGF $\tilde{\mathbf{G}}_c$ with Eq. (11) central region; finally, the new interactor Ω_p is obtained with Eq. (12) to start a new iteration. Such calculation iterates until $\tilde{\mathbf{G}}_{c,p}^Q$ is converged.

In the above, we have introduced the DCA algorithm for calculating the disorder-averaged NEGF. However, the electronic structure self-consistent calculation requires the conditionally averaged GFs, namely, $\tilde{\mathbf{G}}_{c,p,RR}^Q$, for updating the muffin-tin potential for Q element at R (to calculate the quantity D_R^Q). By making use of Eq. (14), we can define, with the cluster GF $\tilde{\mathbf{G}}_{c,p}^Q$,

$$\tilde{\mathbf{G}}_{c,p,BB}^Q = \frac{1}{N_C} \sum_{Q,R} w^Q (\mathbf{G}_{c,p}^Q)_{RR} \eta_{p,R}^{Q,Q} / c_B^Q, \quad (18)$$

where $R = B + \vec{T}_{\parallel}$ denotes the site in the DCA cluster, c_B^Q is the concentration of atom Q on site B , and the occupation operator $\eta_{p,R}^{Q,Q} = 1$ only if site R is occupied by atom Q in the configuration Q , or otherwise $\eta_{p,R}^{Q,Q} = 0$. It can be checked that the following relation is always satisfied:

$$\tilde{\mathbf{G}}_{c,p,BB} = \sum_Q c_B^Q \tilde{\mathbf{G}}_{c,p,BB}^Q. \quad (19)$$

Figure 3 presents the flow chart for the DCA loop embedded in DFT calculation for the nonequilibrium self-consistent calculation. For details about solving the three GFs $G_c^{A/\mathcal{R}/\mathcal{K}}$ related quantities in DCA, see the Appendix.

IV. IMPLEMENTATION OF NEGF BASED FIRST-PRINCIPLES SIMULATION OF DISORDERED DEVICE

We have introduced the algorithm of nonequilibrium DCA in EMTO method for averaging NEGF within the EMTO framework for an operating electronic device with the atomic disorder. In the following, we introduce the quantities required for self-consistent nonequilibrium electronic-structure calculation (for example, electron density, effective muffin-tin potential) and the calculation of disorder-averaged current in DCA.

A. Double-energy contour for the charge density

In the EMTO based DFT self-consistent calculation of disordered device, conditionally averaged charge density $n_B^Q(r_B)$ for the atomic sphere Q at site B is required for updating the potential $V_B^Q(r_B)$ (in muffin-tin approximation) in each

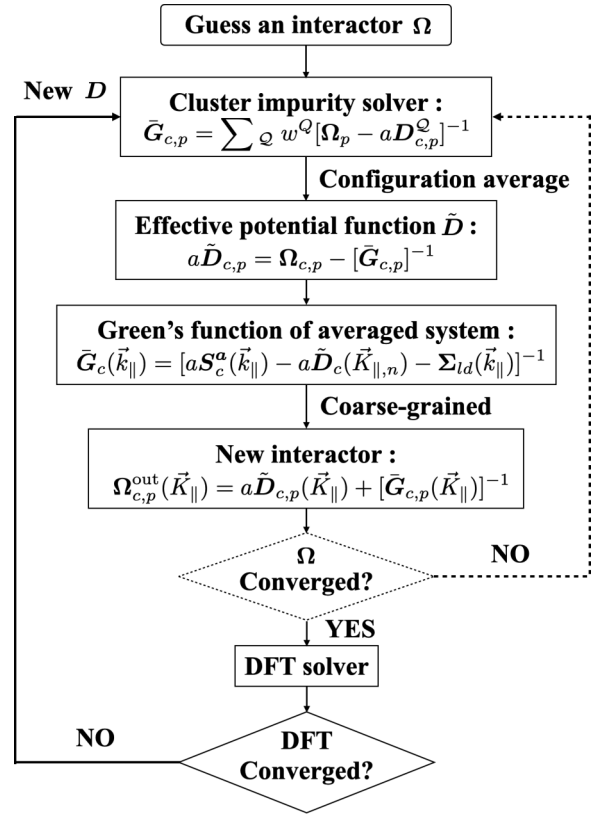


FIG. 3. Flow chart of the EMTO-DFT-NEGF-DCA self-consistent loop for the quantum transport simulation of device materials.

iteration. Generally, $n_B^Q(r_B)$ is composed of contributions from core and valence electrons, namely, $\tilde{n}_B^Q(\vec{r}_B) = \tilde{n}_{B,\text{core}}^Q(r_B) + \tilde{n}_{B,\text{val}}^Q(r_B)$, which are calculated in different ways. $\tilde{n}_{B,\text{core}}^Q(r_B)$ is obtained by directly solving the eigenstates of core levels inside the muffin-tin potential sphere, while valence density $\tilde{n}_{B,\text{val}}^Q$ is evaluated by calculating the NEGF of device region, for example, the lesser GF $\tilde{G}^{<}$.

For valence electrons,

$$\tilde{\rho}_{B,\text{val}}^Q(\vec{r}_B) = \int_{E_{B\text{val}}}^{E_{f,L}} dz \tilde{\rho}_B^{Q,<}(z, \vec{r}_B, \vec{r}_B), \quad (20)$$

where we assume the electrode Fermi energies $E_{f,L} > E_{f,R}$, and $E_{B\text{val}}$ denotes the bottom of valence band. Here the real-space nonequilibrium density (note that we omit the argument \vec{r}_B for convenience in the following)

$$\tilde{\rho}_B^{Q,<}(z) = \frac{1}{2\pi i} \sum_{L,L'} \tilde{G}_{BLBL'}^{Q,<}(z) \phi_{BL}^{a,Q}(z) \phi_{BL'}^{a,Q,\dagger}(z), \quad (21)$$

where $\phi_{BL}^{a,Q}$ is the partial wave for Q element at site B . It is known that $\epsilon < E_{f,R}$, $f_L = f_R = 1$, and $\tilde{\rho}_B^{Q,<}(z)$ thus equal to the equilibrium density matrix, namely, satisfying the fluctuation-dissipation theorem $G^{<} = -2i \text{Im}[G^{\mathcal{R}}]$. Moreover, the $G^{\mathcal{R}}(z)$ has important analytical property in the upper complex energy plane, while $G^{<}$ is only analytical on the real energy axis. As a result, the integration of Eq. (20) is usually performed on a hybrid energy contour, containing $C_{T,1}$

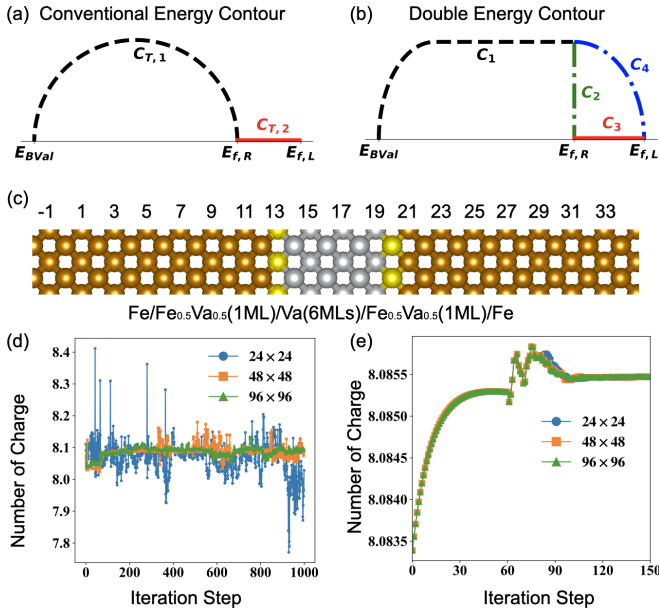


FIG. 4. Schematic illustration of the energy contour for the energy integration in nonequilibrium electron density calculation. (a) The conventional contour is composed of $C_{T,1}$ in the upper complex plane from E_{BVal} to $E_{f,R}$ and $C_{T,2}$ on the real energy axis from $E_{f,R}$ to $E_{f,L}$. (b) Double-energy contours are composed of four parts: C_1 , C_2 , and C_4 in the upper complex energy, and C_3 on the real energy axis from $E_{f,R}$ to $E_{f,L}$. (c) Structure of Fe/Fe_{0.5}Va_{0.5}(1 ML)/Va(6 MLs)/Fe_{0.5}Va_{0.5}(1 ML)/Fe MTJ with disordered interface roughness. (d), (e) For the integrated valence charge versus nonequilibrium self-consistent iterations using the conventional contour (d) and double-energy contour [for the 11th atomic layer in disordered Fe/Va/Fe MTJ as shown in (c) under the bias 1.0 V (starting from the equilibrium potential)]: blue, orange, and green lines are for the calculations with the respective k_{\parallel} meshes of 24×24 , 48×48 , and 96×96 .

in complex energy plane and $C_{T,2}$ (for $E_{f,R} < \epsilon < E_{f,L}$) on real energy axis as shown in Fig. 4(a) [61,68], namely,

$$\bar{n}_B^Q = \int_{C_{T,1}} dz \bar{A}_B^Q(z) + \int_{C_{T,2}} dz \bar{\rho}_B^{<,Q}(z), \quad (22)$$

where $\bar{A}_B^Q(z) = -\frac{1}{\pi} \sum_{L,L'} \text{Im}[\bar{G}_{BLBL'}^{Q,\mathcal{R}}(z)] \phi_{BL}^{a,Q}(z) \phi_{BL'}^{a,Q,\dagger}(z)$.¹ However, $G^{<}$ is a fast-changing function on the real energy axis, the integration in Eq. (22) often presents serious numerical convergence problem, and thus usually involves a large number of k points in the BZ integration, making the nonequilibrium electronic structure self-consistency hard and the computational cost high in comparison with equilibrium calculations.

To overcome this difficulty, it should be noted that the nonequilibrium distribution function $f_B^{\text{NEQ}}(\epsilon)$, for the energy range $E_{f,R} < \epsilon < E_{f,L}$, is close to $f_L = 1$ and $f_R = 0$ for the sites near the respective left and right electrodes and decreases dramatically in the middle part of the device. For example,

¹ $\bar{G}_{BLBL'}^{Q,\mathcal{R}}(z)$ is replaced by $\bar{G}_{BLBL'}^{Q,\mathcal{R}}(z) + \frac{\delta_{L'L}}{a_{Rl} D_{Rl}^Q(z)} \left(\frac{D_{Rl}^Q(z)}{D_{Rl}^Q(\epsilon)} - \sum_{\epsilon_{Rl}^D} \frac{1}{z - \epsilon_{Rl}^D} \right)$ to avoid nonphysical poles.

it is known that $f_B^{\text{NEQ}}(\epsilon) \approx f_{L/R}$ for the sites in the left and right electrode buffer layers. For the sites with $f_B^{\text{NEQ}}(\epsilon) \approx 1$, it is not appropriate to directly integrate $G_{BB}^{<}$ on the real energy axis, but instead we can utilize the relation $G_{BB}^{<} = G_{BB}^A - G_{BB}^{\mathcal{R}} + G_{BB}^{>}$ in which $G^{>}$ is much smaller in magnitude than $G^{<}$. As a result, in the case $f_B^{\text{NEQ}}(\epsilon) \approx 1$, the integration for density can be rewritten as follows, based on a new energy contour as shown in Fig. 4(b):

$$\bar{n}_B^Q = \int_{C_1+C_4} dz \bar{A}_B^Q(z) + \int_{C_3} dz \bar{\rho}_B^{>,Q}(z), \quad (23)$$

where $\bar{\rho}_B^{>,Q}(z) = \frac{1}{2\pi i} \sum_{L,L'} \bar{G}_{BLBL'}^{Q,>}(z) \phi_{BL}^{a,Q}(z) \phi_{BL'}^{a,Q,\dagger}(z)$. Since the second term is quite small, the inaccuracy due to integration on the real axis is negligible, making the calculation of charge density much more accurate than Eq. (22). On the other hand, for the case $f_B^{\text{NEQ}}(z) \approx 0$, with the new contour, the density can be rewritten as, equivalent to Eq. (23),

$$\bar{n}_B^Q = \int_{C_1+C_2} dz \bar{A}_B^Q(z) + \int_{C_3} dz \bar{\rho}_B^{<,Q}(z), \quad (24)$$

where the complex contour $C_1 + C_2$ is equivalent to $C_{T,1}$ as shown in Fig. 4(b). Here, since $G^{<}$ is small, the integration is appropriate, similar to the $G^{>}$ in Eq. (23). To use Eqs. (23) and (24) in practical implementation, we evaluate the distribution function properly as $f_B^{\text{NEQ}}(\epsilon) = \sum_Q c_B^Q \int d\vec{r} \bar{\rho}_B^{Q,<}(\epsilon, \vec{r}) / \int d\vec{r} \bar{A}_B^Q(\epsilon, \vec{r})$ for each site B [it should be mentioned that, since the formulas in Eqs. (23) and (24) are actually equivalent for all sites, no approximation is introduced and this treatment will improve the accuracy of the numerical integration if used properly for different sites]. Then, Eq. (23) is used for $f_B^{\text{NEQ}} > 0.5$, while Eq. (24) is for $f_B^{\text{NEQ}} < 0.5$. In comparison with the conventional contour integration, the computational cost with the new contour in Fig. 4(b) can be importantly reduced with less real-axis energy points and k_{\parallel} points in BZ, making the EMTO-DFT-NEGF-DCA based self-consistent nonequilibrium electronic structure calculation feasible.

To demonstrate the numerical accuracy and efficiency for the integration using the double-energy contour, we make a test for the nonequilibrium self-consistent electronic structure calculation of Fe/Va/Fe magnetic tunneling junction [as shown in above Fig. 4(c) with disordered interfaces under the bias 1.0 V, namely, $E_{f,L} - E_{f,R} = 1.0$ eV]. We compare the integrated number of valence charge for Fe atom at the 11th site with the conventional and double-energy contour. All the calculations start from the same equilibrium potential at zero bias. Figures 4(d) and 4(e) compare the results of the charge versus iteration steps with the respective conventional and double-energy contours using different 2D k_{\parallel} meshes for the integration at real-axis energy (for the information of energy grids and k_{\parallel} mesh, see Ref. [71]). As shown in Fig. 4(d) with the conventional energy contour, it is clear that the result presents large fluctuation versus iteration step due to the important numerical error of k_{\parallel} integration for real-axis energy points. Although the use of dense k_{\parallel} can decrease the magnitude of fluctuation, the numerical convergence is still hard to achieve with even 96×96 k_{\parallel} mesh, making the nonequilibrium self-consistency very difficult to

reach. To fix the convergence problem with conventional energy contour, BZ integration requires a large number of k_{\parallel} points, making the calculation very inefficient. In the contrast, as shown in Fig. 4(e) with the double-energy contour, the results of different k_{\parallel} meshes (24×24 , 48×48 , and 96×96) present negligible differences, and reach the nonequilibrium self-consistency at almost the same iteration steps. Therefore, we can see the use of double-energy contour can significantly reduce the cost for BZ integration while maintaining high accuracy, and thus effectively improve the nonequilibrium electronic structure self-consistency.

B. Effective potential

For the operating device under finite bias, we adopt overlapping potential spheres for each atom Q and spherical cell approximation (SCA) for the muffin-tin potential construction (same as our previous implementation of EMTO for equilibrium electronic structure of two-probe devices) [15,16]. For the central region with open-boundary condition, the effective potential for atomic sphere Q at site B is composed of the three parts, in SCA,

$$V_B^Q(r_B) = V_B^{Q,\text{intra}}(r_B) + V_B^{\text{inter}} + V_B^{\text{bias}}, \quad (25)$$

where $V_B^{Q,\text{intra}}(r_B)$, V_B^{inter} are the potentials describing intracell and intercell interactions, and V_B^{bias} is the correction due to the applied bias potential in the electrodes. $V_B^{Q,\text{intra}}(r_B)$, V_B^{inter} is defined in the same way as the equilibrium cases as in Ref. [15] for a two-probe device. V_B^{bias} is required for satisfying the boundary condition for solving the Poisson equation of the central region. For a given bias V , electrostatic potentials and the associated Fermi energies ($E_{fL/R}$) in the left and right electrodes are shifted by the respective $V/2$ and $-V/2$ in our simulation, which changes the boundary condition of device region compared to the equilibrium case. To be smoothly connected to the electrode potential (for example, in the $+0$ and $N_p + 1$ principal layers), generally, a linear potential drop across the central region should be introduced to match the boundary for biased devices, namely V_B^{bias} (ensured by the uniqueness theorem for the Poisson equation),

$$V_B^{\text{bias}} = -V \left(\frac{z_B}{L} - 0.5 \right), \quad (26)$$

where z_B is the distance from site B to the left interface, and L is the length of the central region along the z axis.

C. Short-range order with DCA

It is known that the different tendency of clustering or anti-clustering of defects [see Fig. 5(e)], namely, short-range order (SRO), due to the different process of realistic nanodevice, could have important influence on the device properties. To study the influence of SRO effect in realistic nanodevice with EMTO-DFT-NEGF-DCA method, we characterize the SRO with the Warren-Cowley parameters [72,73], namely,

$$\alpha_i = \frac{\langle \bar{\Pi}_i \rangle - q^2}{1 - q^2}, \quad (27)$$

where $\langle \bar{\Pi}_i \rangle$ is the averaged pair-correlation function for the i th shell of a site, and q is the concentration difference of the

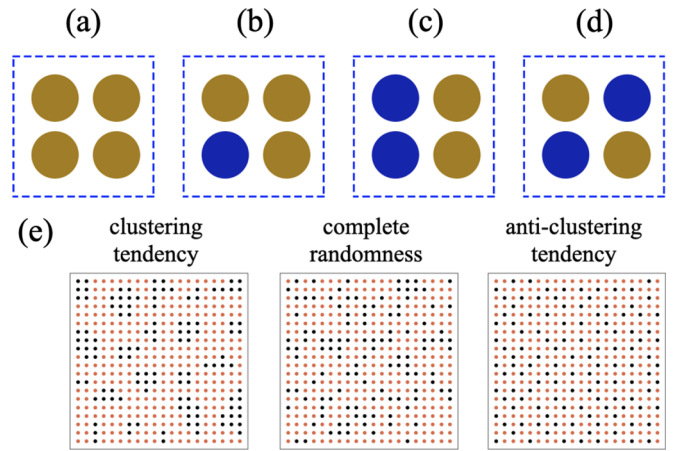


FIG. 5. (a)-(d): the four possible SRO maps for the DCA cluster of $N_{xy} = 4$ and $N_z = 1$. (e) Schematic illustration of SROs with clustering and anticlustering tendencies in comparison with complete randomness.

two elements Q_1 and Q_2 in the binary alloys, namely, $q = c_{Q_1} - c_{Q_2}$. Here, $\bar{\Pi}_i = S_R S_{R+i}$ and $S_R = +1$ (or -1) when site R is occupied by Q_1 (or Q_2) atom. The Warren-Cowley parameter α_i measures the ordering tendency for the presence of the same atom pairs Q_1-Q_1 or Q_2-Q_2 (at R and a site in its i th shell). In particular, $\alpha_i = 0$ describes random distribution of atoms in the i th shell (for the case of complete randomness, $\alpha_i = 0$ for all i), and $\alpha_i > 0$ describes more likely clustering tendency, while $\alpha_i < 0$ describes more likely anticlustering tendency.

To demonstrate our implementation of SRO in DCA, we use the cluster, as an example, with the size of $N_{xy} = 4$ and $N_z = 1$ with four different SRO maps as shown in Fig. 5 (which is also used in our simulation of SRO effects in Fe/Va/Fe MTJ). For each SRO map, we consider all the atomic configurations (with the same weight) under different operation of translation, rotation, and the exchange of Q_1 and Q_2 [for example, we have 2, 8, 4, 2 configurations for the respective map in Figs. 5(a)–5(d)]. We calculate the Warren-Cowley parameters for each SRO map: for Fig. 5(a), $\alpha_1 = 1$ presents the upper limit of clustering tendency; for Fig. 5(d), $\alpha_1 = -1$ presents the upper limit of anticlustering tendency; for Fig. 5(b), $\alpha_1 = 0$ and $\alpha_2 = 0$ presents a tendency close to complete randomness; for Fig. 5(c), $\alpha_1 = 0$ and $\alpha_2 = -1$ presents a random first shell and anticlustering tendency limit in second shell on-equilibrium electronic structure calculation feasible.

D. Averaged transmission in DCA

As known the current formula of Eq. (6) could be rewritten into the form of Landauer-Buttiker formula [74–76]

$$I = \frac{e}{h} \int d\epsilon \mathcal{T}(\epsilon) (f_L - f_R), \quad (28)$$

where $\mathcal{T} = \text{Tr}[G_c^R \Gamma_L G_c^A \Gamma_R]$ is the transmission coefficient. The transmission coefficient \mathcal{T} , accounting for the full quantum interference effect in the device, is the central quantity we target in the EMTO-DFT-NEGF-DCA method for

nanoelectronics simulation. For a disordered device, we calculate the disorder average

$$\bar{\mathcal{T}} = \text{Tr}[\bar{G}_c^R \Gamma_L \bar{G}_c^A \Gamma_R], \quad (29)$$

in which the average of the correlator of G_c^R and G_c^A accounts for the effect of multiple disorder scattering. It can be found that $\bar{\mathcal{T}} = \text{Tr}[-i\bar{G}_c^< \Gamma_R]$ by utilizing the relation $\bar{G}_c^< = i\bar{G}_c^R \Gamma_L \bar{G}_c^A$ for $f_L = 1$ and $f_R = 0$, in which $\bar{G}_c^<$ can be directly known with the NEGF-DCA self-consistent calculation. For further study, the averaged transmission coefficient is separated into two parts: the coherent part, defined as $\bar{\mathcal{T}}_{\text{coh}} = \text{Tr}[\bar{G}_c^R \Gamma_L \bar{G}_c^A \Gamma_R]$ accounts for the specular scattering and the diffusive part, defined as $\bar{\mathcal{T}}_{\text{diff}} = \bar{\mathcal{T}} - \bar{\mathcal{T}}_{\text{coh}}$, presents the contribution of diffusive scattering between different channels. After disorder averaged with DCA, the lattice Fourier transformation can be applied to obtain the \bar{k}_{\parallel} -resolved transmission results, namely,

$$\begin{aligned} \bar{\mathcal{T}}(\bar{k}_{\parallel}) &= \text{Tr}[-i\bar{G}_c^<(\bar{k}_{\parallel})\Gamma_r(\bar{k}_{\parallel})], \\ \bar{\mathcal{T}}_{\text{coh}}(\bar{k}_{\parallel}) &= \text{Tr}[\bar{G}_c^R(\bar{k}_{\parallel})\Gamma_L(\bar{k}_{\parallel})\bar{G}_c^A(\bar{k}_{\parallel})\Gamma_r(\bar{k}_{\parallel})], \\ \bar{\mathcal{T}}_{\text{diff}}(\bar{k}_{\parallel}) &= \bar{\mathcal{T}}(\bar{k}_{\parallel}) - \bar{\mathcal{T}}_{\text{coh}}(\bar{k}_{\parallel}). \end{aligned} \quad (30)$$

V. NUMERICAL RESULTS AND DISCUSSIONS

We have implemented the EMTO-DFT-NEGF-DCA method for first-principles quantum transport simulation of disordered nanoelectronic device, including the calculation of both nonequilibrium electronic structure and transport property. For more details about the self-consistent implementation for device simulation, please refer to Refs. [15,16]. In our previous implementations in Refs. [15,16], we have demonstrated the important accuracy and advantage of the EMTO method for calculating equilibrium electronic structure and electron's charge and spin transport properties of the two-probe device structures. In the following, we will focus on the first-principles NEGF-DCA results for the transport properties and nonequilibrium electronic structure of disordered devices. For the disorder-averaged NEGF with DCA, as an important test of the NEGF-DCA implementation, we have checked that, for $f_L = f_R$ (device is at equilibrium), the fluctuation-dissipation theorem is satisfied, namely, the relation $\bar{G}_c^< = \bar{G}_c^A - \bar{G}_c^R$, illustrating the correct calculation of \bar{G}_c^K with DCA.

In this section, we will first present the transport calculation with a 2D square-lattice tight-binding model, to test the NEGF-DCA formalism for quantum transport simulation of disordered nanodevices. Then, we will present the first-principles DCA results for the electron transport in Cu/Co(111) junction with disordered interface, and spin-dependent tunneling in Fe/Va/Fe junction with surface roughness to demonstrate the disordered cluster and SRO effects on transport. For the equilibrium electronic structure, the conventional semicircle complex contour is adopted with 20 energy points with the Gaussian quadrature method, and 24×24 uniform k mesh is used for the 2D BZ for all the energy points. In the simulation of device under bias, for the non-equilibrium electronic structure, the Gaussian quadrature method is applied on the C_1 , C_2 , and C_4 contours with the respective 12, 6, and 8 energy points and C_3 contour with 8

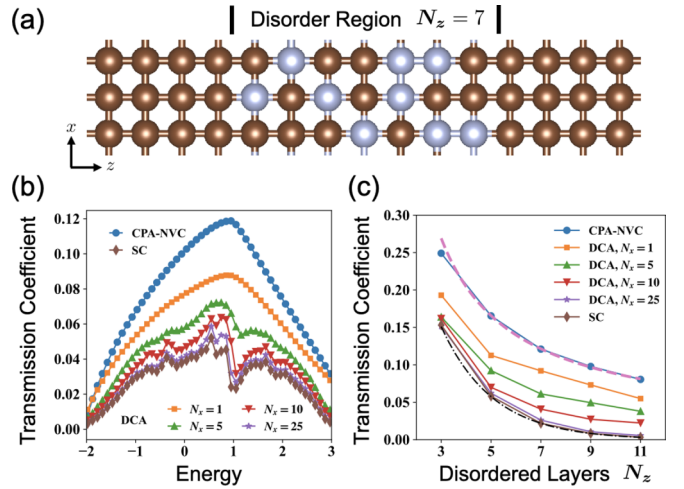


FIG. 6. (a) Schematic illustration of 2D square-lattice model with seven disordered atomic layers along the z direction in the central scattering region. (b), (c) Present the averaged transmission coefficients $\bar{\mathcal{T}}$ with different methods, for the case $\epsilon_{\text{im}} = 10.0$ ($\epsilon_{\text{host}} = 1.0$). (b) For $\bar{\mathcal{T}}$ versus energy for device with seven disordered layers. (c) For $\bar{\mathcal{T}}$ versus disordered layers N_z at energy is equal to 1.0. The pink dashed and black dotted-dashed lines with the respective functions of $A + B/N_z$ and $A \exp(-BN_z) + C$ are fitting to the results of CPA-NVC and SC methods (for understanding the scaling behaviors of different methods).

uniform energy points per eV, and 24×24 uniform k mesh for the 2D BZ is adopted for energy points on C_1 , C_2 , and C_4 . Because the real-axis integration in the second part of Eqs. (23) or (24) on C_3 for different sites is a small quantity, we find the use of the same k mesh as C_4 is sufficient to achieve very good convergence and numerical stability, providing an important advantage for the nonequilibrium electronic structure calculations. Transmission coefficients for energy points on the real axis are calculated with 204×204 k mesh. The local spin density approximation for exchange-correlation functional is employed in all our calculations [77,78]. In the simulation of Fe/Va/Fe junction, the vacuum space is filled with empty spheres.

A. Disorder scattering in 2D square-lattice tight-binding model

To test the NEGF-DCA transport formalism, we compare the averaged transmission $\bar{\mathcal{T}}$ of DCA with different cluster size and the results of supercell method with a 2D disordered square-lattice tight-binding model as shown in Fig. 6(a). The CPA-NVC results in single-site approximation are also included for comparison [1,12,14]. We use the tight-binding Hamiltonian $H = \sum_{(ij)} t(c_i^\dagger c_j + c_j^\dagger c_i) + \sum_i \epsilon_i c_i^\dagger c_i$, where the hopping t is constant and ϵ_i are the disordered onsite energies at site i . Here we consider the nearest neighbor $t = 1.0$, the host $\epsilon_i^{\text{host}} = 1.0$, and the impurity $\epsilon_i^{\text{imp}} = 10.0$ in the central disordered device region. In Figs. 6(b) and 6(c), we present the results for the disorder concentration of 50% which presents the strong scattering effects. The NEGF-DCA calculations take the cluster size $N_z \times N_x$ (N_z is the full length of the central disordered region) and supercell calculation adopts the cell size $N_z \times N_x (= 50)$, and 1000 random atomic

configurations are used in both NEGF-DCA cluster and supercell. Figure 6(b) presents the averaged \bar{T} versus energy for device with $N_z = 7$ disordered layers. As shown, compared to the supercell result, the CPA-NVC presents very large deviation in magnitude in a wide range of energy. For example, at $E = 1.0$, $\bar{T}_{\text{CPA-NVC}}$ is about five times larger than \bar{T}_{SC} , illustrating the important limitation of single-site CPA. However, it is clear that NEGF-DCA provides systematic improvement by increasing the cluster size $N_x (\times N_z)$. It can be found the important improvement over CPA-NVC result can be obtained with NEGF-DCA even with $N_x = 1$. For $N_x = 25$, the NEGF-DCA results present very good agreement with \bar{T}_{SC} , demonstrating the important effectiveness of the NEGF-DCA for treating the correlation effects of strong disorder scattering in quantum transport simulation of nanodevices. Figure 6(c) plots the transmission versus number of disorder layers at the energy $E = 1.0$ using different methods. It is clear that the CPA-NVC results show quite large deviation compared to the NEGF-DCA and supercell results for all the different numbers of disordered layers. However, the results of NEGF-DCA with $N_x = 25$ agree quite well with the supercell calculations. Moreover, it is found that the CPA-NVC results can be fitted well to the function $A + B/N_z$, presenting a behavior of diffusive conductor, while the supercell results obey the behavior of exponential decay, namely, the function $A \exp(-BN_z) + C$, presenting important localization effects. It is clear that the scaling behavior of NEGF-DCA results can become closer and closer to the supercell as increasing the DCA cluster size, presenting the important test for the NEGF-DCA quantum transport method. The test of NEGF-DCA with tight-binding model in Fig. 6 provides an important basis for the first-principles implementation.

B. Effects of nonlocal correlation with DCA in Cu/Co disordered junction

It is known that the single-site CPA provides an effective and accurate method for the cases of weak scattering and low concentration of quenched disorders without SRO, due to the weak nonlocal correlation. However, for the cases of disorders with strong scattering, high concentration and materials and devices made with annealing process, the presence of SRO and strong nonlocal correlations have important influence on the transport properties of materials, which requires a cluster-level description. In this section, we investigate the electron quantum transport in different spin channels in Cu/Cu_{1-x}Co_x/Co (111) junction with disordered interdiffusion. In Fig. 7, we present the transmission coefficient versus disorder concentration with DCA of different cluster sizes and single-site CPA-NVC for comparison. Here, we only consider interfacial disorders Cu_{1-x}Co_x in 2 and 3 atomic monolayers (ML), and arrange all disorders in one principal layer and one DCA cluster, namely, $N_z = 2$ or 3, which is adequate to account for the full nonlocal correlation of disorder scattering in transport direction z . We use the DCA cluster with the disorder in complete randomness.

As we find, the DCA electronic potential presents small difference from single-site CPA results for the Cu/(2/3 ML)Cu_{1-x}Co_x/Co junction. The transmission coefficients are calculated at E_f based on the equilibrium

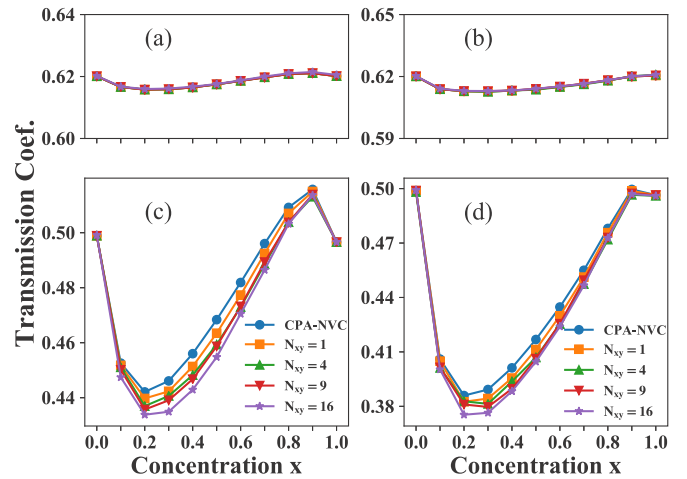


FIG. 7. The total transmission coefficients versus interfacial disorder concentration x in Cu/Cu_{1-x}Co_x/Co (111) junction with two ((a), (c)) and three ((b), (d)) disordered monolayers. Plots (a) and (b) are for the spin-up channel, (c) and (d) are for spin-down channel. Blue circles are for CPA-NVC results, orange squares, green up triangles, red down triangles, and purple stars are for the DCA calculations with the respective $N_{xy}^{\text{DCA}} = 1, 4, 9, \text{ and } 16$.

electronic structure. As presented in Fig. 7 for the Cu/Co(111) junction, it is clear that the nonlocal correlation of interfacial disorders has very different effects on the transmission of spin-up and -down channels. In particular, as seen in Figs. 7(a) and 7(b) for the spin-up channel, the results of single-site CPA-NVC and NEGF-DCA with different cluster size present almost the same results for different disorder concentration x , demonstrating the nonlocal correlations of disorder scattering in both z and x - y directions are weak. In addition, as found in Figs. 7(a) and 7(b), the increased 1-ML disorder presents very limited influence, and all results present small variance versus x (for example, the transmission changes from 0.62 to the minimum 0.614 at $x = 0.25$ for 3-ML disorders), presenting the weak scattering in the spin-up channel.

However, as shown in Figs. 7(c) and 7(d), the transmission of spin-down channel presents important dependence on the disorder concentration for both junctions with 2- and 3-ML disorders. In particular, more than 10% and 20% (maximum) decrease in transmission can be found for junctions with the respective 2- and 3-ML disorders. Moreover, importantly, the difference between single-site CPA-NVC and DCA results is notable for the spin-down channel, presenting the correlation effects of disorder scattering. It is clear that, in comparison with the CPA-NVC result, the inclusion of nonlocal correlation with DCA reduces the transmission, and the transmission decreases with the increase of DCA cluster size, presenting the important localization effects of disorder scattering and an important test for the implementation of DCA for quantum transport simulation of disordered device. It is also found that the transmission tends to converge with increasing the DCA cluster size, consistent with the fact that DCA is exact at infinite cluster size. Since the number of disorder layers (2 and 3 MLs) is very limited in the present calculation, we can only observe limited decrease in the magnitude of transmission, for example, about 5% (maximum) decrease

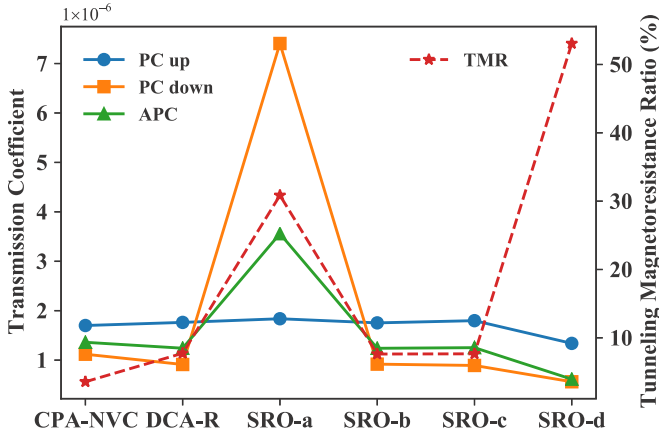


FIG. 8. The total transmission coefficient of different spin channels (left axis) and TMR (right axis) with the CPA-NVC and DCA methods (with various SROs) for Fe/Va/Fe MTJ with surface roughness of $\text{Fe}_{0.5}\text{Va}_{0.5}$.

compared to CPA-NVC results can be found in DCA $N_{xy} = 16$ calculations for both junctions. Another observation is that, at the small concentration x or $1 - x$, the nonlocal correlation of disorder scattering is weak and the single-site CPA-NVC results approach the DCA calculations.

C. Short-range order effects on spin-dependent tunneling in Fe/Va/Fe junction with DCA

In the last section, we present the DCA to account for the nonlocal correlation over the single-site CPA. In this section, we focus on the capability of DCA for including the SRO effects of disorders. As a demonstration, we study the effects of short-range order in Fe/Va/Fe (100) MTJ with disordered surface roughness which usually tends to form local clusters (not in complete randomness). The surface roughness is considered with alloy model $\text{Fe}_x\text{Va}_{1-x}$ where Va denotes vacuum sphere in EMTO. Here, we only consider monolayer surface roughness on the two Fe/Va interfaces (separated by 6-ML vacuum) with the same concentration of $x = 0.5$. (More systematic study of spin-dependent tunneling in Fe/Va/Fe with SRO will be presented in another

work). In present calculations, the DCA cluster of the size $N_z = 1$ and $N_{xy} = 4$ are used with the completely random and SRO configurations as shown in Fig. 5. Figure 8 presents the spin-dependent total transmission for single-site CPA-NVC and DCA with complete randomness (DCA-R) and four different SROs (DCA- $a/b/c/d$). It is clear that the results of APC and spin-down channel in PC can be significantly modulated by the different SROs, while the spin-up channel in PC presents very limited variation in the different calculations. In particular, compared to the single-site CPA-NVC and DCA-R calculations, SRO- a can significantly enhance $T_{\text{PC,down}}$ and T_{APC} ($T_{\text{APC,down}} = T_{\text{APC,up}}$) by about the respective seven and three times, and SRO- d can effectively decrease the results by about two times, while effects of SRO- b and - c almost unchanged the results, presenting very distinct effect of different SROs. It should be noted that the SRO map is largely determined by the fabrication process of materials and devices in experiments. It is already known that the Warren-Cowley parameter $\alpha_1 = 0$ for both SRO- b and - c , denoting the fact that the SRO- b/c maps are close to the complete randomness. However, the fact that $\alpha_1 = 1$ for SRO- a and $\alpha_1 = -1$ for SRO- d tells the respective clustering and anticlustering of defects. As known, the surface relaxation favors the tendency for clustering, and the DCA- a calculation presents the prominent effects of clustering on spin-dependent tunneling. The implementation of NEGF-DCA provides us an effective way to simulate the effects of different SRO on quantum transport through disordered devices. Moreover, in comparison with the single-site CPA-NVC, the inclusion of nonlocal correlation in DCA-R (completely random) only slightly modulates the total transmission in different tunneling channels. In addition, as an important measurement of MTJ's merit, the tunneling magnetoresistance ratio (TMR), namely $\text{TMR} = (T_{\text{PC}} - T_{\text{APC}})/T_{\text{APC}}$, is also shown in Fig. 8. For the MTJ with high concentration disorder $x = 0.5$, DCA-R only slightly increases TMR to 7.7% compared to the CPA-NVC result 3.6%. However, compared to DCA-R result, SRO- a and SRO- d significantly increase the TMR to the respective values 30.85% and 53.07%, while the TMR remains almost unchanged for the cases SRO- b/c .

To further study the effects of different SRO, the k_{\parallel} -resolved transmissions of coherent and diffusive parts,

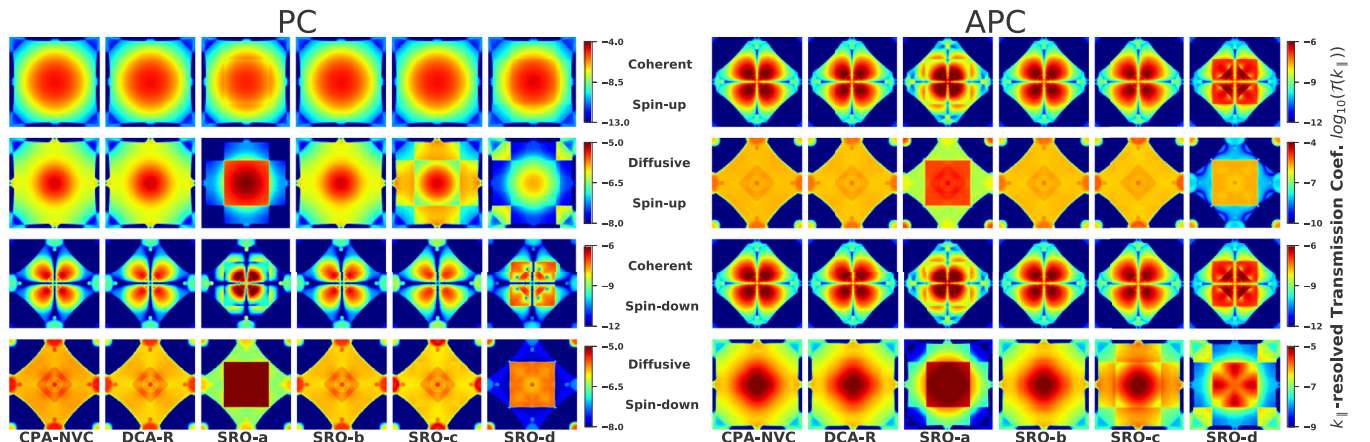


FIG. 9. The k_{\parallel} -resolved transmission (coherent and diffusive parts) of different spin channels in PC and APC with the CPA-NVC and DCA methods (with various SROs) for Fe/Va/Fe MTJ with surface roughness of $\text{Fe}_{0.5}\text{Va}_{0.5}$.

namely, $\bar{T}_{\text{coh}}(\vec{k}_{\parallel})$ and $\bar{T}_{\text{diff}}(\vec{k}_{\parallel})$ in Eq. (30), are presented for the PC and APC in Fig. 9 for different calculations. As shown, for the case of complete randomness, the differences between single-site CPA-NVC and DCA-R results are minor for all spin channels in PC and APC, further demonstrating the weak effects of nonlocal correlation of surface roughness in Fe/Va/Fe MTJ. In the DCA-R transmission results, the coarse-graining induced boundary is not notable, namely, $\tilde{D}_{c,p}(\vec{K}_{\parallel,n})$ is close to $\tilde{D}_{\text{CPA}}(\Gamma)$ for different $\vec{K}_{\parallel,n}$. However, it is found that the patterns of SRO-*a* and -*d* transmissions for both PC and APC present significant difference from the CPA-NVC and DCA-R results, and contain apparent boundaries between different coarse-grained $\vec{K}_{\parallel,n}$ region in 2D BZ, presenting the fact that the $\tilde{D}_{c,p}(\vec{K}_{\parallel,n})$ can vary significantly from each other. The important differences in $\tilde{D}_{c,p}(\vec{K}_{\parallel,n})$ for different $\vec{K}_{\parallel,n}$ reveal the important effects of correlation in SRO-*a* and -*d*. Moreover, it is seen that the short-range order in SRO-*a* significantly enhances the transmission around the Γ point in the diffusive part, resulting in the importance enhancement in the total transmission of spin-down channel in PC and APC as shown in Fig. 8 over DCA-R. On the other hand, compared to the DCA-R, the SRO-*d* result presents important decrease in the transmission away from the Γ point. Furthermore, another observation is that for SRO-*b* and -*c*, transmission patterns and values are all very closed to the results of DCA-R, presenting much weaker SRO effect compare to SRO-*a* and -*d*, consistent with the results in Fig. 8. However, compared to the results of SRO-*b*, the diffusive part of SRO-*c* presents notable differences in patterns for the spin-up channel of PC and spin-down channel of APC, and these important differences can be attributed to the different SRO Warren-Cowley parameters: $\alpha_{1,2} = 0$ for SRO-*b* and $\alpha_1 = 0$, $\alpha_2 = -1$ for SRO-*c*. (The results of SRO-*b* are more close to that of DCA-R). In addition, for different spin channels in APC, the diffusive transmissions present rather different patterns, but they integrate to the same total transmission, providing a test for the present implementation of the NEGF-DCA method. Here, we have seen the important effects of the SRO on spin-dependent tunneling, revealing the effects of different device processes on the device performance. NEGF-DCA provides an important approach to effectively capture the important effects of short-range order on quantum transport through the disordered device.

D. Nonequilibrium electronic structure and transport calculations

In this section, as a further demonstration of the EMTO-DFT-NEGF-DCA method, we present results for the nonequilibrium electronic structure and spin-dependent tunneling calculations in disordered Fe/Va/Fe MTJ with surface roughness under finite bias. In Fig. 10(a), we investigate the nonequilibrium distribution function at different sites, namely, $f_R^{\text{NEQ}} = \text{Tr}[-iG_B^<]/2 \text{Tr}[\text{Im}(G_B^R)]$, for the energy point $E = 0.5(E_{f,L} + E_{f,R})$ in the junction under 1.0-V bias voltage. It is observed that f_R^{NEQ} behaves as a sharp step function, changing quickly from the value almost 1.0 for sites of 1–7 (on the left side including the Fe buffer layer) to the value close to 0.0 for sites of 10–16 (on the right side including the Fe buffer layer).

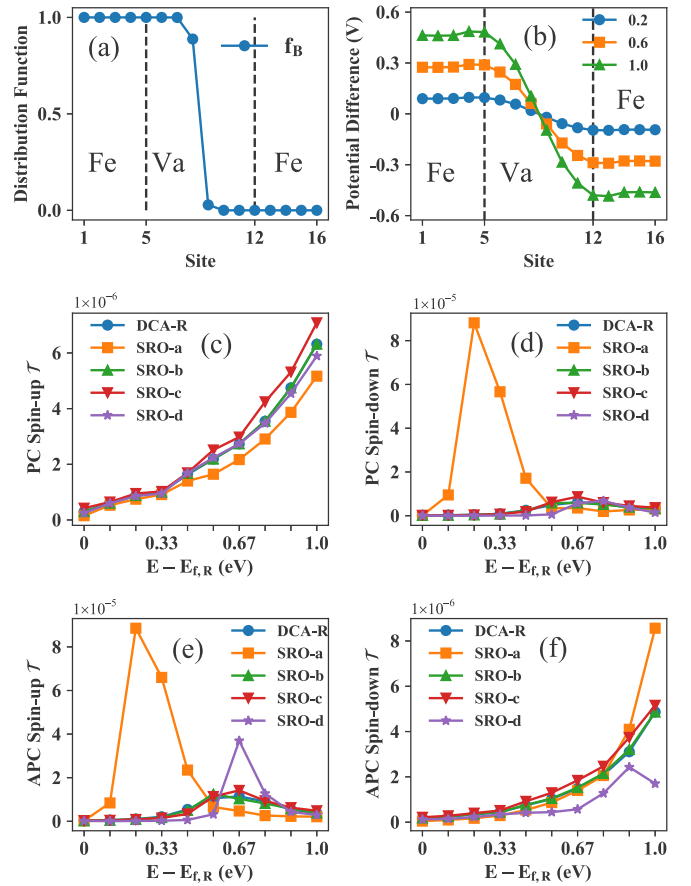


FIG. 10. The nonequilibrium properties of Fe/Va/Fe MTJ with surface roughness of $\text{Fe}_{0.5}\text{Va}_{0.5}$: (a) nonequilibrium distribution function versus sites in the central region for the energy point $E = 0.5 + E_{f,R}$ under the bias voltage 1 V. (b) The potential difference from the equilibrium versus sites in central region: blue circle, orange square, and green up triangle are for the respective applied bias voltages 0.2, 0.6, and 1.0 V. The transmission coefficients versus energy for different spin channels for the bias voltage 1.0 V: (c)–(f) are for the spin-up and -down channels in PC, spin-up, and spin-down channels in APC, respectively.

$f_R^{\text{NEQ}} = 0.89$ for the site 8 while $f_R^{\text{NEQ}} = 0.03$ for site 9. As an important result, the real-axis integration in Eq. (20) on the conventional method is not appropriate for nonequilibrium electron density for atomic spheres at the sites from 1 to 8, while it can be very accurate for integral for sites from 9 to 16. Therefore, the use of the double-energy-contour techniques, including the different treatment of the energy integral for different sites, namely, Eqs. (23) and (24) in which both the integrands on real axis are very small quantities, can greatly improve the numerical convergence, make the DCA based nonequilibrium electronic structure calculations feasible.

Figure 10(b) presents the DCA-R results for the bias-induced potential change ΔV_R for each site, namely, the potential difference between nonequilibrium and equilibrium is given by the bias-induced charge redistribution, for bias voltages of 0.2, 0.6, and 1.0 V. It should be mentioned that, for the electronic potential, the difference between DCA calculations with different clusters and SROs is small for disordered

Fe/Va/Fe MTJ. As shown in Fig. 10(b), it is clear that, for the buffer layer Fe sites from both sides out of the dashed lines, the potential is shifted almost by a constant $\pm \frac{V}{2}$ consistent with the electrode potential shift, while the potential for the Va sites between the dashed lines smoothly connects to the buffer layers potential and decrease almost linearly along the z direction. Our present calculations for different applied biases in Fig. 10(b) produce well the potential behavior in an ideal paralleled-plane capacitor with a vacuum barrier, providing an important test for our implementation of the EMTO-DFT-NEGF-DCA method for the nonequilibrium electronic structure calculations.

Figures 10(c)–10(f) present the transmission results for $E_{f,L} > E > E_{f,R}$ for the Fe/Va/Fe junction under bias voltage 1.0 V. The results of DCA-R and different SRO are compared for different spin channels in PC and APC. For all the calculations, SRO- b transmission (in green) presents almost the same result as DCA-R, illustrating again the SRO- b configurations with $\alpha_1 = 0$, $\alpha_2 = 0$ are close to the complete randomness. Meanwhile, the results of SRO- c (in red) show small deviation from the DCA-R and SRO- b calculations in all spin channels. However, the transmission of SRO- a (in yellow) presents important peaks in the spin-down channel in PC and spin-up channel in APC, which is significantly larger than the other results, presenting abnormal phenomena due to SRO with the clustering tendency in device materials. For example, $T_{PC,down} = 8.8 \times 10^{-5}$ and $T_{APC,up} = 8.9 \times 10^{-5}$ at $E = 0.22$ for SRO- a , compared to the corresponding values 4.2×10^{-7} and 1.0×10^{-6} of DCA-R, while the notable difference between SRO- a and DCA-R can also be found in the other two spin channels. It is also found that the SRO- d with the anticlustering tendency presents important effects in the spin channels of APC, but not in PC (for example, $T_{APC,up}$ reaches a maximum value 3.7×10^{-5} at $E = 0.67$ compared to the DCA-R value 1.1×10^{-5}). Moreover, we calculated the total currents for different spin channels in PC and APC to evaluate $TMR = (I_{PC} - I_{APC})/I_{APC}$, by the integrating the transmission coefficient.² We obtain the TMR value -7.5% and -42.9% for the respective SRO- a and SRO- d , compared to the TMR values -21.7% for DCA-R, -20.7% for SRO- b , and -16.2% for SRO- c . The very different results of different SROs and DCA-R demonstrate the importance of device process and detailed structures for the transport properties of nanoelectronics. The implementation of EMTO-DFT-NEGF-DCA provides an effective approach for studying the process-dependent device and material transport properties from first principles.

VI. CONCLUSIONS

In conclusion, we have developed the EMTO-DFT-NEGF-DCA method, namely, the first-principles nonequilibrium

²The current (in atomic units) of different spin channels for DCA-R, SRO- a – d are as follows: 2.3×10^{-6} , 1.9×10^{-6} , 2.3×10^{-6} , 2.6×10^{-6} , 2.2×10^{-6} for PC spin up, 2.9×10^{-6} , 2.1×10^{-5} , 2.9×10^{-6} , 3.4×10^{-6} , 2.0×10^{-6} for PC spin down, 5.3×10^{-6} , 2.3×10^{-5} , 5.2×10^{-6} , 5.5×10^{-6} , 6.6×10^{-6} for APC spin up, and 1.3×10^{-6} , 1.5×10^{-6} , 1.4×10^{-6} , 1.6×10^{-6} , 7.5×10^{-7} for APC spin down, respectively.

dynamical cluster theory, to simulate the quantum transport through disordered nanoelectronics. In this work, DCA is formulated in the Keldysh's NEGF representation to enable the effective treatment of both the correlation effects of disorder scattering and short-range order effects at nonequilibrium condition. By implementing in the localized and minimal basis EMTO, the present method features high efficiency and accuracy for quantum transport simulation of disordered device materials. In the practical nonequilibrium electronic structure self-consistency, we devise a double-energy-contour technique to increase the numerical convergence in the energy integration, making the simulation of nonequilibrium disordered devices feasible. As an important test, we applied the present EMTO-DFT-NEGF-DCA to calculate the electron transport in Cu/Co junction with interfacial disorder and Fe/Va/Fe MTJ with surface roughness. We find the inclusion of correlations of disorder scattering in very few disordered layers can present a sizable decrease in electron transmission, presenting the important effect of disorder-induced transport channel closing. Moreover, in Fe/Va/Fe MTJ, it is found that the SROs with clustering and anticlustering tendencies can dramatically modulate the spin-dependent transmission properties compared to the case of (or close to) complete randomness, presenting important SRO effects on the device functionality. The development of first-principles nonequilibrium dynamical cluster theory extends the capability of first-principles quantum transport simulation of disordered devices, providing an important approach for the process-dependent device simulation.

ACKNOWLEDGMENTS

Y.K. acknowledges financial support from ShanghaiTech startup, NSFC (Grant No. 11874265). The authors thank the HPC platform of ShanghaiTech University for providing the computational facility.

APPENDIX: SELF-CONSISTENCY FOR NEGF-DCA IN EMTO

In Sec. III, we have introduced the formulation of nonequilibrium DCA in the Keldysh's representation within the EMTO framework for an operating disordered electronic device. However, it is not appropriate to directly solve the DCA equations with 2×2 Keldysh's matrices (containing $\mathcal{A}/\mathcal{R}/\mathcal{K}$ blocks) as a whole. Because of the lower triangular form in the Keldysh's representation, the computation of \mathcal{A}/\mathcal{R} blocks, with the relation of $Q^A = Q^{R,\dagger}$, is independent of the \mathcal{K} block, while \mathcal{K} block is connected with \mathcal{A}/\mathcal{R} blocks. In practical implementation, for the energy contours of C_1 , C_2 , and C_4 , only the G_c^R is required for each energy point. For C_3 , we need calculate all the $G_c^{R/A/\mathcal{K}}$ to obtain $G_c^{</>}$ containing the nonequilibrium quantum statistics in Eqs. (23) and (24). For the DCA cluster solver, namely Eqs. (14) and (15), we can rewrite them explicitly as

$$\begin{aligned} G_{c,p}^{R/A,Q} &= [\Omega_p^{R/A} - aD_{c,p}^Q]^{-1}, \\ G_{c,p}^{\mathcal{K},Q} &= -G_{c,p}^{R,Q} \Omega_p^{\mathcal{K}} G_{c,p}^{A,Q}, \\ \bar{G}_{c,p}^{A/\mathcal{R}/\mathcal{K}} &= \sum_Q w^Q G_{c,p}^{A/\mathcal{R}/\mathcal{K},Q}, \end{aligned} \quad (A1)$$

where $G_{c,p}^{A,\mathcal{Q}} = G_{c,p}^{\mathcal{R},\mathcal{Q},\dagger}$. Then, based on the known averaged $\bar{G}_{c,p}^{A/\mathcal{R}/\mathcal{K}}$, $\bar{D}_{c,p}^{A/\mathcal{R}/\mathcal{K}}$ in real space can be obtained with Eq. (16) explicitly as

$$\begin{aligned} a\bar{D}_{c,p}^{\mathcal{R}/A} &= \Omega_p^{\mathcal{R}/A} - [\bar{G}_{c,p}^{\mathcal{R}/A}]^{-1}, \\ a\bar{D}_{c,p}^{\mathcal{K}} &= \Omega_p^{\mathcal{K}} + (\bar{G}_{c,p}^{\mathcal{R}})^{-1} \bar{G}_{c,p}^{\mathcal{K}} (\bar{G}_{c,p}^A)^{-1}. \end{aligned} \quad (\text{A2})$$

With the Fourier transformed to $\vec{K}_{\parallel,n}$ representation, we obtain explicitly with Eq. (17)

$$\bar{D}_{c,p,B,B'}^{\mathcal{R}/A/\mathcal{K}}(\vec{K}_{\parallel,n}) = \sum_{\vec{T}_{\parallel}} e^{-i\vec{K}_{\parallel,n} \cdot \vec{T}_{\parallel}} [\bar{D}_{c,p}^{\mathcal{R}/A/\mathcal{K}}]_{B,B'+\vec{T}_{\parallel}}. \quad (\text{A3})$$

The averaged GF $\bar{G}_c^{A/\mathcal{R}/\mathcal{K}}(\vec{k}_{\parallel})$ of the central region can be calculated explicitly with the known $\bar{D}_{c,p}^{\mathcal{R}/\mathcal{K}}$ as

$$\begin{aligned} \bar{G}_c^{\mathcal{R}}(\vec{k}_{\parallel}) &= [aS_c^{a,\mathcal{R}}(\vec{k}_{\parallel}) - a\bar{D}_c^{\mathcal{R}}(\vec{K}_{\parallel,n}) - \Sigma_{ld}^{\mathcal{R}}(\vec{k}_{\parallel})]^{-1}, \\ \bar{G}_c^{\mathcal{K}}(\vec{k}_{\parallel}) &= \bar{G}_c^{\mathcal{R}}(\vec{k}_{\parallel}) [a\bar{D}_c^{\mathcal{K}}(\vec{K}_{\parallel,n}) + \Sigma_{ld}^{\mathcal{K}}(\vec{k}_{\parallel})] \bar{G}_c^A(\vec{k}_{\parallel}). \end{aligned} \quad (\text{A4})$$

After applying the coarse-grained approximation, $\bar{G}_{c,p}^{A/\mathcal{R}/\mathcal{K}}(\vec{K}_{\parallel,n}) = \frac{1}{N_{\vec{k}_{\parallel}}} \sum_{\vec{k}_{\parallel}} \bar{G}_{c,p}^{A/\mathcal{R}/\mathcal{K}}(\vec{K}_{\parallel,n} + \vec{k}_{\parallel})$, we generate new coherent interactor explicitly with Eq. (12) as follows:

$$\begin{aligned} \Omega_p^{\mathcal{R}}(\vec{K}_{\parallel,n}) &= [\bar{G}_{c,p}^{\mathcal{R}}(\vec{K}_{\parallel,n})]^{-1} + a\bar{D}_{c,p}^{\mathcal{R}}(\vec{K}_{\parallel,n}), \\ \Omega_p^{\mathcal{K}}(\vec{K}_{\parallel,n}) &= a\bar{D}_{c,p}^{\mathcal{K}}(\vec{K}_{\parallel,n}) - [G_{c,p}^{\mathcal{R}}]^{-1} G_{c,p}^{\mathcal{K}} [G_{c,p}^A]^{-1}(\vec{K}_{\parallel,n}). \end{aligned}$$

-
- [1] Y. Ke, K. Xia, and H. Guo, *Phys. Rev. Lett.* **105**, 236801 (2010).
[2] J. Yan, S. Wang, K. Xia, and Y. Ke, *Phys. Rev. B* **95**, 125428 (2017).
[3] P. Soven, *Phys. Rev.* **156**, 809 (1967).
[4] D. W. Taylor, *Phys. Rev.* **156**, 1017 (1967).
[5] V. Drchal, J. Kudrnovský, and I. Turek, *Comput. Phys. Commun.* **97**, 111 (1996).
[6] P. E. A. Turchi, G. M. Stocks, W. H. Butler, D. M. Nicholson, and A. Gonis, *Phys. Rev. B* **37**, 5982 (1988).
[7] N. H. Long and H. Akai, *J. Phys.: Condens. Matter* **19**, 365232 (2007).
[8] L. Vitos, I. A. Abrikosov, and B. Johansson, *Phys. Rev. Lett.* **87**, 156401 (2001).
[9] L. Vitos, I. A. Abrikosov, and B. Johansson, Coherent potential approximation within the exact muffin-tin orbitals theory, in *Complex Inorganic Solids: Structural, Stability, and Magnetic Properties of Alloys*, edited by P. E. A. Turchi, A. Gonis, K. Rajan, and A. Meike (Springer, Boston, 2005), pp. 339–352.
[10] L. Vitos, *Computational Quantum Mechanics for Materials Engineers: The EMTO Method and Applications* (Springer, London, 2007).
[11] F. Tian, L. K. Varga, J. Shen, and L. Vitos, *Comput. Mater. Sci.* **111**, 350 (2016).
[12] Y. Ke, K. Xia, and H. Guo, *Phys. Rev. Lett.* **100**, 166805 (2008).
[13] Y. Ke, F. Zahid, V. Timoshevskii, K. Xia, D. Gall, and H. Guo, *Phys. Rev. B* **79**, 155406 (2009).
[14] J. Yan and Y. Ke, *Phys. Rev. B* **94**, 045424 (2016).
[15] Q. Zhang, J. Yan, Y. Zhang, and Y. Ke, *Phys. Rev. B* **100**, 075134 (2019).
[16] Z. Chen, Q. Zhang, Y. Zhang, L. Wang, M. Sang, and Y. Ke, *Phys. Rev. B* **102**, 035405 (2020).
[17] B. Velický, S. Kirkpatrick, and H. Ehrenreich, *Phys. Rev.* **175**, 747 (1968).
[18] T. K. G. Nambodhiri, C. J. McMahon, and H. Herman, *Metall. Trans.* **4**, 1323 (1973).
[19] B. P. Burton, E. Cockayne, and U. V. Waghmare, *Phys. Rev. B* **72**, 064113 (2005).
[20] I. Jankowska-Sumara, M. Paściak, M. Kądziołka-Gaweł, M. Podgórna, A. Majchrowski, and K. Roleder, *J. Phys.: Condens. Matter* **32**, 435402 (2020).
[21] X. Liu, Y. Wang, Q. Guo, S.-J. Liang, T. Xu, B. Liu, J. Qiao, S. Lai, J. Zeng, S. Hao, C. Gu, T. Cao, C. Wang, Y. Wang, C. Pan, G. Su, Y. Nie, X. Wan, L. Sun, Z. Wang *et al.*, *Phys. Rev. Mater.* **5**, L041001 (2021).
[22] A. Zunger, S. H. Wei, L. G. Ferreira, and J. E. Bernard, *Phys. Rev. Lett.* **65**, 353 (1990).
[23] M. Tsukada, *J. Phys. Soc. Jpn.* **26**, 684 (1969).
[24] M. Tsukada, *J. Phys. Soc. Jpn.* **32**, 1475 (1972).
[25] A. Gonis, *Green Functions for Ordered and Disordered Systems* (North-Holland, Amsterdam, 1992).
[26] M. H. Hettler, A. N. Tahvildar-Zadeh, M. Jarrell, T. Pruschke, and H. R. Krishnamurthy, *Phys. Rev. B* **58**, R7475 (1998).
[27] M. H. Hettler, M. Mukherjee, M. Jarrell, and H. R. Krishnamurthy, *Phys. Rev. B* **61**, 12739 (2000).
[28] M. Jarrell and H. R. Krishnamurthy, *Phys. Rev. B* **63**, 125102 (2001).
[29] R. Moradian, B. L. Györfy, and J. F. Annett, *Phys. Rev. Lett.* **89**, 287002 (2002).
[30] D. A. Rowlands, J. B. Staunton, and B. L. Györfy, *Phys. Rev. B* **67**, 115109 (2003).
[31] D. Rowlands, *J. Phys.: Condens. Matter* **18**, 3179 (2006).
[32] G. M. Batt and D. Rowlands, *J. Phys.: Condens. Matter* **18**, 11031 (2006).
[33] U. Yu, A.-M. Nili, K. Mielsons, B. Moritz, J. Moreno, and M. Jarrell, *Phys. Rev. Lett.* **104**, 037201 (2010).
[34] J. A. Blackman, D. M. Esterling, and N. F. Berk, *Phys. Rev. B* **4**, 2412 (1971).
[35] W. R. Mondal, T. Berlijn, M. Jarrell, and N. S. Vidhyadhiraja, *Phys. Rev. B* **99**, 134203 (2019).
[36] S.-X. Yang, H. Terletska, Z. Y. Meng, J. Moreno, and M. Jarrell, *Phys. Rev. E* **88**, 063306 (2013).
[37] C. E. Ekuma, H. Terletska, Z. Y. Meng, J. Moreno, M. Jarrell, S. Mahmoudian, and V. Dobrosavljević, *J. Phys.: Condens. Matter* **26**, 274209 (2014).
[38] C. E. Ekuma, H. Terletska, K.-M. Tam, Z.-Y. Meng, J. Moreno, and M. Jarrell, *Phys. Rev. B* **89**, 081107(R) (2014).
[39] H. Terletska, Y. Zhang, L. Chioncel, D. Vollhardt, and M. Jarrell, *Phys. Rev. B* **95**, 134204 (2017).
[40] Y. Zhang, Y. F. Zhang, S. X. Yang, K.-M. Tam, N. S. Vidhyadhiraja, and M. Jarrell, *Phys. Rev. B* **95**, 144208 (2017).

- [41] J. Velev and W. H. Butler, *J. Appl. Phys.* **97**, 10C517 (2005).
- [42] T. B. Boykin, M. Luisier, A. Schenk, N. Kharche, and G. Klimeck, *IEEE Trans. Nanotechnol.* **6**, 43 (2007).
- [43] P. Hohenberg and W. Kohn, *Phys. Rev.* **136**, B864 (1964).
- [44] W. Kohn and L. J. Sham, *Phys. Rev.* **140**, A1133 (1965).
- [45] D. A. Rowlands, A. Ernst, B. L. Györfy, and J. B. Staunton, *Phys. Rev. B* **73**, 165122 (2006).
- [46] D. A. Rowlands, X. G. Zhang, and A. Gonis, *Phys. Rev. B* **78**, 115119 (2008).
- [47] D. A. Rowlands, *Rep. Prog. Phys.* **72**, 086501 (2009).
- [48] P. R. Tulip, J. B. Staunton, S. Lowitzer, D. Ködderitzsch, and H. Ebert, *Phys. Rev. B* **77**, 165116 (2008).
- [49] O. K. Andersen, C. Arcangeli, R. W. Tank, T. Saha-Dasgupta, G. Krier, O. Jepsen, and I. Dasgupta, *Mater. Res. Soc. Symp. Proc.* **491**, 3 (1997).
- [50] O. K. Andersen and T. Saha-Dasgupta, *Phys. Rev. B* **62**, R16219 (2000).
- [51] L. Vitos, H. Skriver, B. Johansson, and J. Kollár, *Comput. Mater. Sci.* **18**, 24 (2000).
- [52] H. Haug and A.-P. Jauho, *Quantum Kinetics in Transport and Optics of Semiconductors* (Springer, Berlin, 2008).
- [53] One-particle Green's function, in *Nonequilibrium Many-Body Theory of Quantum Systems: A Modern Introduction*, edited by G. Stefanucci and R. van Leeuwen (Cambridge University Press, Cambridge, 2013), pp. 153–204.
- [54] R. A. Craig, *J. Math. Phys.* **9**, 605 (1968).
- [55] L. V. Keldysh, *Sov. Phys.—JETP* **20**, 1018 (1965).
- [56] Y. Meir and N. S. Wingreen, *Phys. Rev. Lett.* **68**, 2512 (1992).
- [57] J. Taylor, H. Guo, and J. Wang, *Phys. Rev. B* **63**, 121104(R) (2001).
- [58] J. Taylor, H. Guo, and J. Wang, *Phys. Rev. B* **63**, 245407 (2001).
- [59] Y. Xue, S. Datta, and M. A. Ratner, *J. Chem. Phys.* **115**, 4292 (2001).
- [60] Y. Xue, S. Datta, and M. A. Ratner, *Chem. Phys.* **281**, 151 (2002).
- [61] M. Brandbyge, J.-L. Mozos, P. Ordejón, J. Taylor, and K. Stokbro, *Phys. Rev. B* **65**, 165401 (2002).
- [62] S.-H. Ke, H. U. Baranger, and W. Yang, *Phys. Rev. B* **70**, 085410 (2004).
- [63] S. V. Faleev, F. Léonard, D. A. Stewart, and M. van Schilfgaarde, *Phys. Rev. B* **71**, 195422 (2005).
- [64] A. R. Rocha, V. M. García-suárez, S. W. Bailey, C. J. Lambert, J. Ferrer, and S. Sanvito, *Nat. Mater.* **4**, 335 (2005).
- [65] W. Lu, V. Meunier, and J. Bernholc, *Phys. Rev. Lett.* **95**, 206805 (2005).
- [66] D. Waldron, P. Haney, B. Larade, A. MacDonald, and H. Guo, *Phys. Rev. Lett.* **96**, 166804 (2006).
- [67] O. K. Andersen, T. Saha-Dasgupta, R. W. Tank, C. Arcangeli, O. Jepsen, and G. Krier, in *Electronic Structure and Physical Properties of Solids*, edited by H. Dreyssé (Springer, Berlin, 2000), pp. 3–84.
- [68] I. Turek, V. Drchal, J. Kudrnovský, M. Šob, and P. Weinberger, *Electronic Structure of Disordered Alloys, Surfaces and Interfaces* (Springer, Boston, 1997).
- [69] E. M. Godfrin, *J. Phys.: Condens. Matter* **3**, 7843 (1991).
- [70] F. Brouers, M. Cyrot, and F. Cyrot-Lackman, *Phys. Rev. B* **7**, 4370 (1973).
- [71] We use 28 energy points on the $C_{T,1}$ part of conventional-energy contour, and 12, 8, 8 energy points on the respective C_1 , C_2 , and C_4 parts of double-energy contour, and use $24 \times 24k_{\parallel}$ mesh for these complex contour energy points, and 10 energy points with 24×24 , 48×48 , and 96×96 different k_{\parallel} meshes on the $C_{T,2}$ and C_3 real-axis parts.
- [72] J. M. Cowley, *J. Appl. Phys.* **21**, 24 (1950).
- [73] C. Wolverton, V. Ozoliņš, and A. Zunger, *Phys. Rev. B* **57**, 4332 (1998).
- [74] R. Landauer, *IBM J. Res. Dev.* **1**, 223 (1957).
- [75] M. Büttiker, *Phys. Rev. Lett.* **57**, 1761 (1986).
- [76] S. Datta, *Quantum Transport: Atom to Transistor* (Cambridge University Press, Cambridge, 2005).
- [77] D. M. Ceperley and B. J. Alder, *Phys. Rev. Lett.* **45**, 566 (1980).
- [78] J. P. Perdew and A. Zunger, *Phys. Rev. B* **23**, 5048 (1981).